

Correlated helimagnetic configuration in a nonsymmorphic magnetic nodal semimetal

Xi Luo^{1,*}, Yu-Ge Chen^{2,*}, Ye-Min Zhan³, and Yue Yu^{3†}

1. College of Science,
University of Shanghai for Science and Technology,
Shanghai 200093, China

2. Institute for Quantum Science and Technology,
Department of Physics, Shanghai University,
Shanghai 200444, China

3. State Key Laboratory of Surface Physics and Department of Physics,
Fudan University, Shanghai 200433, China

(Dated: September 10, 2025)

Nonsymmorphic magnetic Weyl semimetal materials such as ReAlX (Re=rare earth, X=Si/Ge) provide a unique opportunity to explore the correlated phenomena between Weyl fermions and nontrivial magnetic configurations. To be specific, we study a lattice model in which the magnetic configuration is determined by the competition among ferromagnetic (FM) interaction, the Dzyaloshinskii-Moriya interaction, and the Kondo coupling K_0 to the Weyl fermion. Both quantum and finite-temperature phase transitions between FM and correlated nesting helical configurations are found. Different from the uncorrelated helimagnet that decouples from the Weyl fermions, this correlated helimagnet induces a magnetic Brillouin zone with a K_0 -dependent nesting in the band structure of the conduction electrons instead of the monopole-like Weyl cone. By measuring the current induced by the chiral magnetic effect on the conduction electron with nesting Weyl nodes, one can distinguish the correlated nesting helical order from the ferromagnetism because the chiral magnetic effect is considerably suppressed in the former case. These properties we find here may explain the experimental observations in ReAlX.

I. INTRODUCTION

Recently, the nodal semimetals in a set of nonsymmorphic magnetic materials, ReAlX (Re=rare earth, X=Si/Ge), attract widespread attention [1–4] and a type of Weyl semimetals with breaking of both the time-reversal Θ and inversion P symmetries was found in ReAlX [5–14]. These magnetic materials belong to the body-centered tetragonal crystal system with a non-centrosymmetric space group $I4_1md$. Due to the P breaking, the Weyl nodes possess different energies. Meanwhile, the f -orbital electrons of the rare earth elements provide a strong magnetic moment, so that a strong Ruderman-Kittel-Kasuya-Yosida (RKKY) interaction can exist by mediating Weyl fermions. The RKKY interaction induces competition among the Heisenberg, Kitaev-Ising, and Dzyaloshinskii-Moriya (DM) interactions [15–19], which leads to the emergence of several nontrivial magnetic configurations, such as spiral, helical, hedgehog, skyrmion, and meron-antimeron pairs [20].

The ReAlX materials provide a unique opportunity to study the correlated phenomena that come from the interplay between Weyl fermions and nontrivial magnetic configurations through the Kondo coupling [21], e.g., new exotic phenomena such as the topological Hall effect and room temperature anomalous Hall effect [10, 12]. This raises the possibility of preparing high-density ultra-fast

storage devices with these materials [22–26].

Physically, those nontrivial magnetic orders rotate the Weyl fermion's spin configuration in real space via the Kondo coupling, which competes with the monopole topology of the Weyl nodes in momentum space. This competition may further induce new correlated phenomena and correlated topological states of matter that lack clear explanations thus far.

In this paper, we focus on the correlated nesting helical magnetic configuration (CNHMC), which has been observed in ReAlX materials. For example, since the ratio between out-of-plane and in-plane magnetic susceptibility χ_c/χ_a is very close in SmAlSi at 2K, a helimagnet with $\mathbf{Q} = \frac{2\pi}{3}(0.979, 0.979, 0)$ emerges, which is consistent with the nesting vector between Weyl nodes [10]. In CeAlGe, a phase transition from the canted magnetic order to the helimagnet was observed at 4.5K. The helimagnet also provides a nesting vector between the Weyl nodes and stabilizes magnetic fluctuations from the magnetic transition temperature to the Curie temperature [9]. This phase transition to the helimagnet and the CNHMC effect are also reported for PrAlSi [5], NdAlSi [6, 7], CeAlSi [8], and NdAlGe [11].

However, the mechanism of the magnetic phase transition and the origin of the emergence of the CNHMC in those materials remain unclear. The specific mechanism behind the anomalous transport phenomena observed near $T = 12.8\text{K}$ in CeAlGe [9], such as the nearly zero magnetoresistance, the switch from negative to positive magnetoresistance, and the maximal suppression of thermal conductivity by magnetic fields is not yet fully understood. In Ref. [9], in which two of the present authors

*These two authors contribute equally.

†Correspondence to: yuyue@fudan.edu.cn

participated, a phenomenological analysis was conducted by treating the magnetic order and Weyl fermions separately (termed uncorrelated Weyl node nesting), while the CNHMC effects and magnetic phase transition remain unexplored.

Conventionally, the magnetic configuration \mathbf{M} and Weyl fermions are separately studied. However, in ReAlX, the strong Kondo coupling plays an important role, so this separated treatment is not valid. In this paper, we develop an exact solution to the Kondo coupling problem in the continuum limit, identifying a characteristic zero-energy mode at the Fermi surface associated with helical magnetic ordering. We then take this correlated \mathbf{M} configuration as a background field to deal with the conduction electrons. When we determine the phase diagram of the correlated magnetism, we fix the fermion spin configuration. With these approximations, we see the phase transitions from an ordered phase, e.g., the ferromagnetic (FM) one, to the CNHMC both at zero temperature and finite temperature. We calculate the current induced by the chiral magnetic effect (CME) both in the FM phase and the CNHMC and find that the current for the latter is an order of magnitude less than that for the former. This may explain the nearly zero magnetoresistance near $T = 12.8\text{K}$ in CeAlGe [9].

The rest of this paper is organized as follows. In Sec. II, we construct a minimal two-band model for a Weyl semimetal that breaks both time-reversal and inversion symmetries and is coupled to the magnetic configuration \mathbf{M} . We also consider the continuum limit of the model with the helical magnetic configuration, and an exact solution is found at zero energy. In Sec. III, we draw the band structures of the lattice model with CNHMC and find that the band structure forms a magnetic Brillouin zone, and the Weyl nodes are folded onto each other for small Kondo coupling. For large Kondo coupling, the Weyl nodes move towards each other, eventually annihilating and opening a gap. In this section, we also consider the magnetic phase diagram by calculating the ground state energy per site at zero temperature and the free energy per site at finite temperature. We find a competition between the ferromagnetic phase and the helical one, which is consistent with the experiments. In Sec. IV, we calculate the CME of the lattice model. We find that the corresponding magnetoresistance of CNHMC is strongly suppressed compared to that of the ferromagnetic case, which may relate to the nearly zero magnetoresistance observed in CeAlGe [9]. The final part is devoted to conclusions.

II. LATTICE MODEL AND CONTINUUM LIMIT

A. Lattice model

The common model study for the materials ReAlX starts from the calculation of the band structure of

this body-centered tetragonal crystal system with a non-centrosymmetric space group $I4_1md(109)$. The Weyl nodes are found near the Fermi level and are coupled to the local moment from the f electron in the rare-earth element. Such a strategy is fine but it is difficult to understand the basic physics due to the complicated numerics.

Due to the crystal symmetry and observed large anomalous Hall effects [5, 8, 11–13], the conduction electrons in ReAlX are Weyl semimetals with both Θ and P symmetry breaking. Remarkably, ReAlX-type materials exhibit dramatic changes in transport properties (e.g., magnetoresistance) across the phase transition to the helimagnetically ordered state. To see the basic physics behind the numerics, we study a simplified cubic lattice model in which the conduction electrons are Weyl semimetals without Θ and P symmetries and have two Weyl nodes that are adjusted to be near the Fermi level. The electrons couple to \mathbf{M}_i via the Kondo coupling while the nearest neighbor \mathbf{M}_i and \mathbf{M}_j are coupled through the FM Heisenberg and the DM interactions:

$$\begin{aligned} H &= H_W + H_K + H_H + H_{DM}, \\ H_W &= \sum_j [(-t_x c_j^\dagger \sigma_z c_{j+\hat{x}} - t_y c_j^\dagger \sigma_z c_{j+\hat{y}} - t_z c_j^\dagger \sigma_z c_{j+\hat{z}} \\ &\quad - it'_x c_j^\dagger \sigma_x c_{j+\hat{x}} - it'_y c_j^\dagger \sigma_y c_{j+\hat{y}} - iv_0 c_j^\dagger \sigma_0 c_{j+\hat{z}} \\ &\quad + h.c.) + m c_j^\dagger \sigma_z c_j], \\ H_K &= \sum_j K_0 \mathbf{s}_j \cdot \mathbf{M}_j, \quad H_H = \sum_{\langle ij \rangle} J_0 \mathbf{M}_i \cdot \mathbf{M}_j, \\ H_{DM} &= \sum_{\langle ij \rangle} \mathbf{D}_0 \cdot \mathbf{M}_i \times \mathbf{M}_j. \end{aligned} \quad (1)$$

For simplicity, we restrict H_W to be a minimal two-band model [27, 28] and the Weyl nodes are located at $(0, 0, \pm k_0)$ with $\cos k_0 = (m/2 - t_x - t_y)/t_z$. c_j^\dagger (the spin index omitted) is the creation operator of the conduction electron at site j with spin $\mathbf{s}_j = \frac{1}{2} c_j^\dagger \boldsymbol{\sigma} c_j$. For the FM case, $J_0 < 0$. In the following, we use $t_x = t_y = t_z = t'_x = t'_y = t = 1, m = 5t$ and $k_0 = \pi/3$. The chemical potential has been set to zero. H_K is the on-site Kondo coupling between \mathbf{s}_i and \mathbf{M}_i with the coupling strength K_0 . H_H and H_{DM} are the nearest-neighbor FM Heisenberg and DM interactions, respectively, both originating from RKKY coupling between Weyl fermions and rare-earth local moments. Although our simplified model adopts a cubic lattice, we can map it to the tetragonal symmetry $I4_1md$ through parameter tuning. Specifically, tuning $t_x = t_y \neq t_z$ and $t'_x = t'_y$ and substituting $k_z \rightarrow \frac{a}{c} k_z$ (where $a \neq c$ are the xy -plane and z -direction lattice constants) reproduces the ReAlX structure. The typical parameters in ReAlX are $a \sim 4 \text{ \AA}$, $c \sim 14 \text{ \AA}$, $t_{x,y} \sim 100 \text{ meV}$, and $t_z \sim 70 \text{ meV}$ [5–11]. For clarity in studying CNHMC's topological properties, we use an isotropic model. Our simulations demonstrate that CNHMC-induced band folding significantly suppresses the CME, while reproducing the experimentally observed magnetoresistance trends in Re-

AlX compounds.

Beyond the helical magnetic order, other complex magnetic configurations (e.g., canted orders) and physical phenomena emerge due to multiple Weyl node pairs and lattice non-symmorphic features, though these are beyond our present scope. Our work concentrates on the ferromagnetic-to-helical phase transition and its topological characteristics, while a four-band model addressing multiple Weyl pairs will be developed in future studies.

When solving the conduction electron problem, we use the adiabatic approximation, i.e., assuming the conduction electrons are fast-moving with respect to the fluctuations of \mathbf{M} when \mathbf{M} is considered a background. On the other hand, the configuration of \mathbf{M} is determined by the competition of the variational ground state energies when the conduction electron spin is assumed to be polarized by \mathbf{M} 's configuration, the CNHMC or ferromagnet.

For the helical magnetic configuration, without loss of generality, one takes $\mathbf{M} = (\sin[Qz], \cos[Qz], 0)$. The Hamiltonian for Weyl fermions with the Kondo coupling becomes

$$\begin{aligned} H_0 &= H_W + H_K \\ &= \sum_{\mathbf{k}, \sigma} [(m - 2t_x \cos k_x - 2t_y \cos k_y \\ &\quad - 2t_z \cos k_z) c_\sigma^\dagger(\mathbf{k}) \sigma_z c_\sigma(\mathbf{k}) + 2t'_x \sin k_x c_\sigma^\dagger(\mathbf{k}) \sigma_x c_\sigma(\mathbf{k}) \\ &\quad + 2t'_y \sin k_y c_\sigma^\dagger(\mathbf{k}) \sigma_y c_\sigma(\mathbf{k}) + 2v_0 \sin k_z c_\sigma^\dagger(\mathbf{k}) \sigma_0 c_\sigma(\mathbf{k}) \\ &\quad + (c_\uparrow^\dagger(k_x, k_y, Q + k_z) (-i \frac{K_0}{2}) c_\downarrow(k_x, k_y, k_z) + h.c.)], \end{aligned} \quad (2)$$

where \uparrow and \downarrow are the spin indices. The last term in Eq. (2) is the Kondo coupling between the Weyl fermion and the helical magnetic configuration. Notice that the momentum shift from k_z to $k_z \pm Q$ comes from the helical wave number Q .

B. Continuum limit and CNHMC effects

To demonstrate the energetic preference for helical ordering in Kondo-coupled Weyl systems, we first establish its stability in the continuum limit [Eq. (2)] before validating with lattice simulations, and demonstrate that the correlated helimagnet constitutes an allowed ground-state configuration. When $|Q| \ll 2|k_0|$, due to the energy offset b_0 between the two Weyl nodes in a non-centrosymmetric system, we can integrate out one Weyl fermion that is below the chemical potential, say, ψ_- . The effective equations of motion of \mathbf{M} and the conduction electron $\psi = \psi_+$ at a given Weyl valley in the continuum limit are given by [29]

$$\begin{aligned} -i\boldsymbol{\sigma} \cdot (\nabla + i \frac{K_0}{2} \mathbf{M}) \psi &= E_e \psi, \\ K_0 \mathbf{s} + \frac{D}{2} \nabla \times \mathbf{M} - J \nabla^2 \mathbf{M} &= 0, \end{aligned} \quad (3)$$

where $J \propto K_0^2 - 2J_0$ and $D \propto v_- K_0^2 + 4D_0$ [15, 16]. In the correlated case, the helimagnet remains an exact

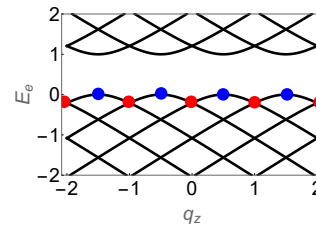


FIG. 1: (color online) The energy spectrum in the continuum limit for Weyl fermions coupled with a helimagnet along the q_z -direction. We set $Q = K_0 = 1$. The helimagnet introduces a magnetic Brillouin zone. The red points stand for the Weyl nodes and the blue points stand for the zero modes (see Appendix A).

$E_e = 0$ solution with $Q = \frac{D \pm \sqrt{D^2 + 16|J|K_0}}{4|J|}$, which reduces to the uncorrelated helimagnet or the ferromagnet when $K_0 = 0$ i.e., $Q = |\mathbf{Q}| = |D/2J|$ and/or $Q = 0$ [30]. When $K_0 \neq 0$, \mathbf{M} and ψ are correlated via the Kondo coupling. The energy spectrum of the conduction electron ψ is shown in Fig. 1. The zero mode solutions are localized at the boundaries of the magnetic Brillouin zone which is introduced due to the helimagnet (for details, see Appendix A).

When \mathbf{Q} of the helimagnet forms a commensurate nesting vector between the Weyl nodes, the helimagnet becomes a CNHMC. This nesting effect has been used to explain the experimental results in CeAlGe [9], but the uncorrelated helimagnet state is not available in ReAlX. By considering the CNHMC, the low-energy effective Hamiltonian of the conduction electron reads $H'_{eff} = \sum_{\mathbf{k}} \Phi_{\mathbf{k}}^\dagger h'_{\mathbf{k}} \Phi_{\mathbf{k}}$, where

$$\begin{aligned} h'_{\mathbf{k}} &= k'_x \sigma_x \tau_0 + k'_y \sigma_y \tau_0 + k'_z \sigma_z \tau_z \\ &\quad + a_0 k'_z \sigma_0 \tau_0 + b_0 \sigma_0 \tau_z + K_0 \sigma_y \tau_x / 2, \end{aligned} \quad (4)$$

and $\Phi = (c_{+\uparrow}, c_{+\downarrow}, c_{-\uparrow}, c_{-\downarrow})$ with \pm labeling two Weyl valleys; σ and τ are the matrices that act on spin and valley indices, respectively. $k'_x = 2t'_x k_x$, $k'_y = 2t'_y k_y$, $k'_z = 2t_z (\sin k_0) k_z$, $a_0 = v_0 (\cot k_0) / t$, and $b_0 = 2v_0 (\sin k_0)$. The spectra of Hamiltonian (4) read

$$\begin{aligned} E_{\pm, \pm} &= a_0 k'_z \pm \\ &\quad \sqrt{k'^2 + (K_0/2)^2 + b_0^2 \pm \sqrt{K_0^2 (k_y'^2 + k_z'^2) + 4b_0^2 k'^2}} \end{aligned} \quad (5)$$

In the $K_0 \rightarrow 0$ limit, b_0 becomes the energy offset between the two Weyl nodes, and a_0 controls the type of the Weyl node. When $b_0 \rightarrow 0$, the CNHMC does not open a gap but drives the Weyl semimetal to a nodal-riding semimetal when $k_y'^2 + k_z'^2 = K_0^2/4$.

III. BAND STRUCTURE AND PHASE DIAGRAM

A. Band structures of the fermion

We now turn back to the lattice model. Similar to dealing with integer quantum Hall effects with the lattice model [31–33] (also see Appendix B for a brief review), one defines $|\Psi\rangle = \sum_{j=1}^q \psi_j c^\dagger(k_x, k_y, k_z^0 + Qj)|0\rangle$, where $Q = 2\pi p/q$ with p and q coprime, $k_z = k_z^0 + Qj$, and $\psi_{j+q} = \psi_j$. Then, the Schrödinger equation $H_0|\Psi\rangle = E|\Psi\rangle$ is reduced to the Harper equations

$$\begin{aligned} & [m - 2t_x \cos k_x - 2t_y \cos k_y - 2t_z \cos(k_z^0 + Qj)]\sigma_z \psi_j \\ & + 2t'_x \sin k_x \sigma_x \psi_j + 2t'_y \sin k_y \sigma_y \psi_j + 2v_0 \sin(k_z^0 + Qj)\psi_j \\ & + (i\frac{K_0}{2})((\frac{\sigma_z - 1}{2})\psi_{j-1} + (\frac{\sigma_z + 1}{2})\psi_{j+1}) \\ & = E(k_x, k_y, k_z^0)\psi_j. \end{aligned} \quad (6)$$

The Harper equations have q eigenvalues for a given (k_x, k_y, k_z^0) . The original band is split into q subbands due to the Kondo coupling to the CNHMC, and each subband has a reduced magnetic Brillouin zone: $-\pi \leq k_x, k_y \leq \pi$ and $-\pi/q \leq k_z^0 \leq \pi/q$.

In ReAlX, the Fermi velocity is $\sim 1\text{eV}\text{\AA}$, and the lattice constant is $\sim 10\text{\AA}$, and then $t \sim 100\text{meV}$. The Curie temperature is about 30K , and then $|J_0| \sim 2.5\text{meV}$. From the first-principles calculations, $|K_0| \sim |D_0| \sim |J_0|$ are of the same order [5–14]. With these parameters, we plot the band structures of H_0 (2) with the CNHMC in Fig. 2. The observed helimagnetic ordering in SmAlSi with nesting vector $\mathbf{Q} = \frac{2\pi}{3}(0.979, 0.979, 0)$ [10] motivates our choice of the commensurate $Q = 2\pi/3$ ($1/3$ Brillouin zone length) as the Weyl node nesting vector. We find that, for the commensurate nesting $Q = 2\pi/3$, the Weyl nodes are folded to the boundaries of the magnetic Brillouin zone for a small K_0 (see Fig. 2a). The monopole charges of the left and right Weyl nodes (red points) in Fig. 2b are -1 and $+1$, whereas the monopole charges of the other band crossings induced by the band folding of CNHMC are zero. This topological feature is also confirmed by Fermi arc states under open-boundary conditions in Fig. 2c. As K_0 increases, the Weyl nodes move towards each other (see Fig. 2b), which may explain the slightly incommensurate behavior of the helimagnetic configuration observed in experiments [10]. For a strong enough K_0 , the Weyl nodes merge together and finally open a gap. The Fermi arcs that connect the Weyl nodes will also evolve from shortening to disappearing; see Fig. 2c (for more details, see Appendix C). These phenomena reflect the competition between the monopole topology of the Weyl node in momentum space and the trivial topology of the helimagnet in real space. The P -breaking term v_0 shifts the energy of every Weyl node and does not alter the location of the Weyl nodes (see Fig. 2d).

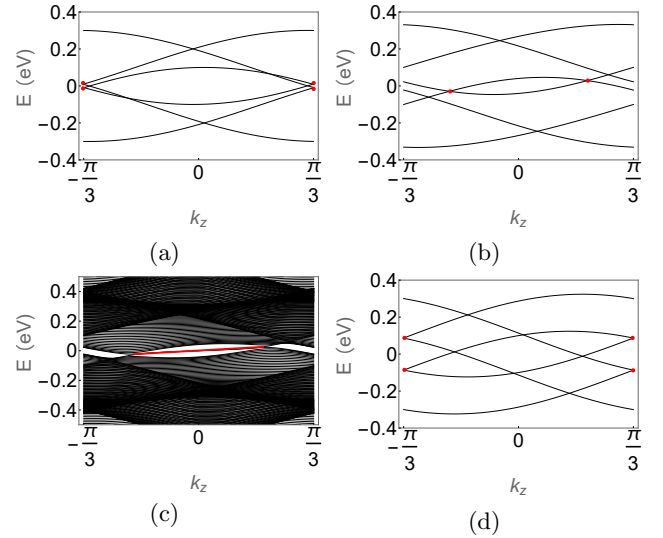


FIG. 2: (color online) The band structures of Weyl fermions with CNHMC for parameters $Q = 2\pi/3$, $t = t' = 0.1\text{ eV}$, and $k_x = k_y = 0$. (a) $K_0 = 10\text{ meV}$. (b) $K_0 = 200\text{ meV}$. (c) Open boundary conditions for (b) with 50 sites along the y axis. (d) $K_0 = 10\text{ meV}$. Parameter values: (a-c) $v_0 = 5\text{ meV}$ and (d) $v_0 = 50\text{ meV}$. The red points in (a), (b), and (d) indicate the Weyl nodes. The red line in (c) represents the Fermi arc.

B. Magnetic phase diagram

We turn to study the magnetic phase diagrams of the model Hamiltonian (1). For a fixed magnetic configuration, which is either the ferromagnet or the CNHMC, we compare the ground state energy per site at zero temperature and the free energy f per site at finite temperature of Eq. (1). For the CNHMC, one takes $Q = 2\pi/3$ and the ferromagnet is given by $Q = 0$. To obtain the spectra, we use exact diagonalization in the calculations and choose periodic boundary conditions for a cubic lattice with $L_x = L_y = L_z = 20$.

At zero temperature, we find that for a fixed J_0 , the CNHMC is favored for large DM interaction D_0 . The phase boundary moves downward when K_0 increases (see Fig. 3a). At finite temperature, by choosing $J_0 = -3\text{meV}$, $D_0 = -4\text{meV}$, $K_0 = 10\text{meV}$, with the other parameters the same as those in Fig. 2a, a phase transition occurs at about $T_c = 4.5\text{K}$ (Fig. 3b), which is qualitatively consistent with experiments in Ref. [9], although the ordered phase is a canted magnetic order instead of the ferromagnet. By increasing K_0 , T_c also increases (see Fig. 3b).

IV. CME WITH CNHMC

To further explore the effects of the CNHMC in this type of magnetic Weyl semimetals, we study the CME [34]. For an isolated Weyl node given by the low-energy Hamiltonian $h_w = b_0 + \sigma \cdot (\mathbf{k} - \mathbf{b})$, where \mathbf{b} and b_0 denote

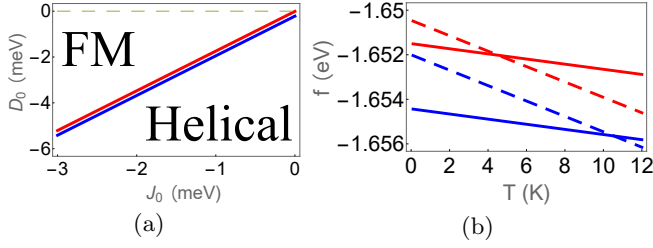


FIG. 3: (color online) The parameters are the same as in Fig. 2a except for K_0 . $K_0 = 10\text{meV}$ for the red lines and $K_0 = 50\text{meV}$ for the blue lines. (a) The zero-temperature phase diagram with J_0 vs D_0 . The gray dashed line stands for the case with $D_0 = 0$, for which the ground state energy per site is the same for both phases along the lines. Above (below) the lines, the FM (helical) configuration is energetically favored. (b) The free energy per site f vs temperature T for $J_0 = -3\text{meV}$ and $D_0 = -4\text{meV}$. The solid (dashed) lines stand for f with the FM (helical) configuration.

the shift in momentum and energy, respectively. Its response to the external magnetic field is described by the topological θ term, $\theta_{\mathbf{r},t}\mathbf{E} \cdot \mathbf{B}$, with $\theta_{\mathbf{r},t} = 2(\mathbf{b} \cdot \mathbf{r} - b_0 t)$ [35–38], which originates from the chiral anomaly of the Weyl fermion [39–41] and corresponds to the charge density $\rho \propto \mathbf{b} \cdot \mathbf{B}$ and current $\mathbf{j} \propto (\mathbf{b} \times \mathbf{E} - b_0 \mathbf{B})$. The \mathbf{b} -related terms contribute to the anomalous Hall effect, while the b_0 term contributes to the CME which is related to the giant negative magnetoresistance [42–45]. In our model Hamiltonian (2), $b_0 \propto v_0$ and $\mathbf{b} \propto (0, K_0, 0)$ in the FM limit $Q = 0$. For the CNHMC with $|Q| = 2|k_0|$, \mathbf{b} is not well defined for small K_0 because the Weyl nodes are close to each other due to band folding.

To explore the CME with the CNHMC, we apply a uniform magnetic field in the z direction in the Hamiltonian (2). In the x - y plane, the lattice sites are labeled by (n, m) , and the gauge $\theta_{(n,m),(n+1,m)}^x = 0$ and $\theta_{(n,m),(n,m+1)}^y = 2\pi\phi n$ is used [31–33]. Under this gauge, the flux through a unit plaquette is $2\pi\phi$. The current arising from the CME reads [42]

$$J_z = \sum_{n,k_y,k_z} \langle \phi_{n,k_y,k_z} | \frac{\partial H_0(k_z)}{\partial k_z} | \phi_{n,k_y,k_z} \rangle n_F(E_n(k_y, k_z)), \quad (7)$$

where n_F is the Fermi distribution function. The periodic boundary conditions in the y and z directions are used. Both periodic and open boundary conditions are considered in the x direction with a length L_x . We set $\phi = 1/5$.

To see the CME in Weyl semimetals, a cutoff $\Lambda \ll \pi$ in the summation of k_z is taken instead of summing over the whole Brillouin zone and the current grows linearly in b_0 for a Weyl semimetal [42]. With this scenario, we calculate the CME with $L_x = 20$, $\Lambda = \pi/6$, and plot J_z by varying v_0 and K_0 at zero temperature in Fig. 4. We find that the Fermi arc states have a negative contribution to J_z because J_z under open boundary conditions is slightly smaller than that under periodic conditions. In

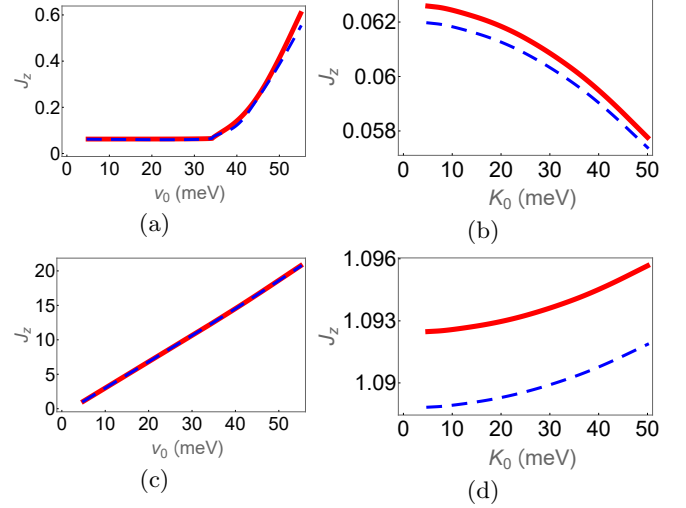


FIG. 4: (color online) The current J_z of the CME at zero temperature with $t = t' = 0.1\text{eV}$, $\phi = 1/5$, and $L_x = 20$ is shown with periodic boundary conditions for the red solid lines and open boundary conditions for the blue dashed lines. $\Lambda = \pi/6$. (a) $K_0 = 10\text{meV}$, $Q = 2\pi/3$; (b) $v_0 = 5\text{meV}$, $Q = 2\pi/3$; (c) $K_0 = 10\text{meV}$, $Q = 0$; (d) $v_0 = 5\text{meV}$, $Q = 0$.

the FM case, J_z is linearly dependent on v_0 as expected (see Fig. 4c), while for the CNHMC, J_z remains a constant when $v_0 < 3K_0$ and then grows (see Fig. 4a). For a large v_0 , the folded Weyl nodes are separated far enough and isolated (see Fig. 2d). Therefore, the linear behavior of J_z versus v_0 is expected. In the J_z constant regime, J_z decreases when K_0 increases. This shows that the Kondo coupling suppresses the CME with the CNHMC (see Fig. 4b) while it raises the CME with the FM order (see Fig. 4d). The key observation is that the CME in the CNHMC is about 20 times smaller than that in the FM order, which may explain the nearly zero behavior observed near $T = 12.8\text{K}$ in CeAlGe [9].

V. CONCLUSIONS

We constructed a minimal lattice model with Kondo, FM, and DM interactions for the Weyl semimetal in which both Θ and P symmetries are broken, which caught the key correlated physics in ReAlX. We found that the CNHMC induces a magnetic Brillouin zone in the band structure of the conduction electrons. The magnetic phase transitions from the ordered phase to the CNHMC were explored. We also calculated the CME with the CNHMC, which is about 20 times smaller than that with the FM order. This may provide an explanation for the anomalous transport phenomena and nearly zero magnetoresistance observed in CeAlGe.

Acknowledgments

The authors thank Long Liang and Yong-Shi Wu for useful discussions. This work is supported by the National Natural Science Foundation of China with Grant No. 12174067 (XL, YMZ, and YY).

DATA AVAILABILITY

The data that support the findings of this article are not publicly available. The data are available from the authors upon reasonable request.

-
- [1] S.-Y. Xu, N. Alidoust, G.-Q. Chang, H. Lu, B. Singh, I. Belopolski, D. S. Sanchez, X. Zhang, G. Bian, H. Zheng, M.-A. Hsuanu, Y. Bian, S.-M. Huang, C.-H. Hsu, T.-R. Chang, H.-T. Jeng, A. Bansil, T. Neupert, V. N. Strocov, H. Lin, S. Jia, M. Z. Hasan, "Discovery of Lorentz-violating type II Weyl fermions in LaAlGe", *Sci. Adv.* **3**, e1603266 (2017).
 - [2] G.-Q. Chang, B. Singh, S.-Y. Xu, G. Bian, S.-M. Huang, C.-H. Hsu, I. Belopolski, N. Alidoust, D. S. Sanchez, H. Zheng, H. Lu, X. Zhang, Y. Bian, T.-R. Chang, H.-T. Jeng, A. Bansil, H. Hsu, S. Jia, T. Neupert, H. Lin, and M. Z. Hasan, "Magnetic and noncentrosymmetric Weyl fermion semimetals in the RAlGe family of compounds (R = rare earth)", *Phys. Rev. B* **97**, 041104(R) (2018).
 - [3] D. S. Sanchez, G. Chang, I. Belopolski, H. Lu, J.-X. Yin, N. Alidoust, X. Xu, T. A. Cochran, X. Zhang, Y. Bian, S. S. Zhang, Y.-Y. Liu, J. Ma, G. Bian, H. Lin, S.-Y. Xu, S. Jia, and M. Z. Hasan, "Observation of Weyl fermions in a magnetic non-centrosymmetric crystal", *Nat. Commun.* **11**, 3356 (2020).
 - [4] D. Destraz, L. Das, S. S. Tsirkin, Yang Xu, T. Neupert, J. Chang, A. Schilling, A. G. Grushin, J. Kohlbrecher, L. Keller, P. Puphal, E. Pomjakushina and J. S. White, "Magnetism and anomalous transport in the Weyl semimetal PrAlGe: possible route to axial gauge fields", *npj Quantum Mater.* **5**, 5 (2020).
 - [5] H.-Y. Yang, B. Singh, B. Lu, C.-Y. Huang, F. Bahrami, W.-C. Chiu, D. Graf, S.-M. Huang, B. Wang, H. Lin, D. Torchinsky, A. Bansil, and F. Tafti, "Transition from Intrinsic to Extrinsic Anomalous Hall Effect in the ferromagnetic Weyl Semimetal PrAlGe_{1-x}Si_x", *APL Mater.* **8**, 011111 (2020).
 - [6] J. Gaudet, H.-Y. Yang, S. Baidya, B. Lu, G. Xu, Y. Zhao, J. A. Rodriguez-Rivera, C. M. Hoffmann, D. E. Graf, D. H. Torchinsky, P. Nikolić, D. Vanderbilt, F. Tafti, and C. L. Broholm, "Weyl-mediated helical magnetism in NdAlSi", *Nat. Mater.* **20**, 1650 (2021).
 - [7] R. Yamada, T. Nomoto, A. Miyake, T. Terakawa, A. Kikkawa, R. Arita, M. Tokunaga, Y. Taguchi, Y. Tokura, and M. Hirschberger, "Nernst effect of high-mobility Weyl electrons in NdAlSi enhanced by a fermi surface nesting instability", *Phys. Rev. X* **14**, 021012 (2024).
 - [8] H.-Y. Yang, B. Singh, J. Gaudet, B. Lu, C.-Y. Huang, W.-C. Chiu, S.-M. Huang, B. Wang, F. Bahrami, B. Xu, J. Franklin, I. Sochnikov, D. E. Graf, G. Xu, Y. Zhao, C. M. Hoffman, H. Lin, D. H. Torchinsky, C. L. Broholm, A. Bansil, and F. Tafti, "Noncollinear ferromagnetic Weyl Semimetal with Anisotropic Anomalous Hall Effect", *Phys. Rev. B* **103**, 115143 (2021).
 - [9] N. C. Drucker, T. Nguyen, F. Han, P. Siriviboon, X. Luo, N. Andrejevic, Z. Zhu, G. Bednik, Q. T. Nguyen, Z. Chen, L. K. Nguyen, T. Liu, T. J. Williams, M. B. Stone, A. I. Kolesnikov, S. Chi, J. Fernandez-Baca, C. S. Nelson, A. Alatas, T. Hogan, A. A. Puretzky, S. Huang, Y. Yu, and M. Li, "Topology stabilized fluctuations in a magnetic nodal semimetal", *Nat. Commun.* **14**, 5182 (2023).
 - [10] X. Yao, J. Gaudet, R. Verma, D. E. Graf, H.-Y. Yang, F. Bahrami, R. Zhang, A. A. Aczel, S. Subedi, D. H. Torchinsky, J. Sun, A. Bansil, S.-M. Huang, B. Singh, P. Blaha, P. Nikolić, and F. Tafti, "Large Topological Hall Effect and Spiral Magnetic Order in the Weyl Semimetal SmAlSi", *Phys. Rev. X* **13**, 011035 (2023).
 - [11] H.-Y. Yang, J. Gaudet, R. Verma, S. Baidya, F. Bahrami, X. Yao, C.-Y. Huang, L. DeBeer-Schmitt, A. A. Aczel, G. Xu, H. Lin, A. Bansil, B. Singh, and F. Tafti, "Stripe helical magnetism and two regimes of anomalous Hall effect in NdAlGe", *Phys. Rev. Materials* **7**, 034202 (2023).
 - [12] A. Laha, A. K. Kundu, N. Aryal, E. S. Bozin, J. Yao, S. Paone, A. Rajapitamahuni, E. Vescovo, T. Valla, M. Abeykoon, R. Jing, W. Yin, A. N. Pasupathy, M. Liu, and Q. Li, "Electronic structure, magnetic and transport properties of antiferromagnetic Weyl semimetal GdAlSi", *Phys. Rev. B* **109**, 035120 (2024).
 - [13] N. Kikugawa, S. Uji, and T. Terashima, "Anomalous Hall effect in the magnetic Weyl semimetal NdAlGe with plateaus observed at low temperatures", *Phys. Rev. B* **109**, 035143 (2024).
 - [14] J. Nag, B. Das, S. Bhowal, Y. Nishioka, B. Bandyopadhyay, S. Kumar, K. Kuroda, A. Kimura, K. G. Suresh, and A. Alam, "GdAlSi: An antiFM topological Weyl semimetal with non-relativistic spin splitting", *Phys. Rev. B* **110**, 224436 (2024).
 - [15] H.-R. Chang, J. Zhou, S.-X. Wang, W.-Y. Shan, and D. Xiao, "RKKY interaction of magnetic impurities in Dirac and Weyl semimetals", *Phys. Rev. B* **92**, 241103(R) (2015).
 - [16] M. V. Hosseini and M. Askari, "Ruderman-Kittel-Kasuya-Yosida interaction in Weyl semimetals", *Phys. Rev. B* **92**, 224435 (2015).
 - [17] J.-H. Sun, D.-H. Xu, F.-C. Zhang, and Y. Zhou, "Magnetic impurity in a Weyl semimetal", *Phys. Rev. B* **92**, 195124 (2015).
 - [18] S.-X. Wang, H.-R. Chang, and J. Zhou, "RKKY interaction in three-dimensional electron gases with linear spin-orbit coupling", *Phys. Rev. B* **96**, 115204 (2017).
 - [19] Me. Zhou, H.-R. Chang, L. Yang, and L. Liang, "Weyl-mediated Ruderman-Kittel-Kasuya-Yosida interaction revisited: imaginary-time formalism and finite temperature effects", *Phys. Rev. B* **112**, 054449 (2025).
 - [20] B. Göbel, I. Mertig, O. A. Tretiakov, "Beyond skyrmions: Review and perspectives of alternative magnetic quasiparticles", *Physics Reports* **895**, 1 (2021).
 - [21] A. K. Mitchell and L. Fritz, "Kondo effect in three-dimensional Dirac and Weyl systems", *Phys. Rev. B* **92**, 121109(R) (2015).

- [22] B. A. Bernevig, C. Felser, and H. Beidenkopf, "Progress and prospects in magnetic topological materials", *Nature* **603**, 41 (2022).
- [23] Z. Wang, Y. Su, S.-Z. Lin, and C. D. Batista, "Meron, Skyrmion, and Vortex Crystals in Centrosymmetric Tetragonal Magnets", *Phys. Rev. B* **103**, 104408 (2021).
- [24] J. Repicky, P.-K. Wu, T. Liu, J. P. Corbett, T. Zhu, S. Cheng, A. S. Ahmed, N. Takeuchi, J. Guerrero-Sanchez, M. Randeria, R. K. Kawakami, and J. A. Gupta, "Atomic-Scale Visualization of Topological Spin Textures in the Chiral Magnet MnGe", *Science* **374**, 1484 (2021).
- [25] S. Luo and L. You, "Skyrmion Devices for Memory and Logic Applications", *APL Mater.* **9**, 050901 (2021).
- [26] V. Rogers, S. Chaudhary, R. Nguyen, and J. A. Incorvia, "Bulk axial Landau levels in the helically magnetized Weyl Hamiltonian and application to multistate memory devices", *Phys. Rev. B* **109**, 115159 (2024).
- [27] F.-Y. Li, X. Luo, X. Dai, Y. Yu, F. Zhang, and G. Chen, "Hybrid Weyl semimetal", *Phys. Rev. B* **94**, 121105(R) (2016).
- [28] T. M. McCormick, I. Kimchi, and N. Trivedi, "Minimal models for topological Weyl semimetals", *Phys. Rev. B* **95**, 075133 (2017).
- [29] Y. Yu, "Seiberg-Witten monopoles: Weyl metal coupled to chiral magnets", arXiv: 1605.00093.
- [30] N. Nagaosa, X. Z. Yu, Y. Tokura, "Gauge fields in real and momentum spaces in magnets: monopoles and skyrmions", *Phil. Trans. R. Soc. A* **370**, 5806 (2012).
- [31] M. Kohmoto, "Zero modes and the quantized Hall conductance of the two-dimensional lattice in a magnetic field", *Phys. Rev. B* **39**, 11943 (1989).
- [32] Y. Hatsugai and M. Kohmoto, "Energy spectrum and the quantum Hall effect on the square lattice with next-nearest-neighbor hopping", *Phys. Rev. B* **42**, 8282 (1990).
- [33] Y. Hatsugai, "Edge states in the integer quantum Hall effect and the Riemann surface of the Bloch function", *Phys. Rev. B* **48**, 11851 (1993).
- [34] K. Fukushima, D. E. Kharzeev, and H. J. Warringa, "Chiral magnetic effect", *Phys. Rev. D* **78**, 074033 (2008).
- [35] A. A. Zyuzin and A. A. Burkov, "Topological response in Weyl semimetals and the chiral anomaly", *Phys. Rev. B* **86**, 115133 (2012).
- [36] D. T. Son and N. Yamamoto, "Berry Curvature, Triangle Anomalies, and the Chiral Magnetic Effect in Fermi Liquids", *Phys. Rev. Lett.* **109**, 181602 (2012).
- [37] P. Goswami and S. Tewari, "Axionic field theory of (3+1)-dimensional Weyl semimetals", *Phys. Rev. B* **88**, 245107 (2013).
- [38] A. G. Grushin, "Consequences of a condensed matter realization of Lorentz-violating QED in Weyl semi-metals", *Phys. Rev. D* **86**, 045001 (2012).
- [39] S. L. Adler, "Axial-Vector Vertex in Spinor Electrodynamics", *Phys. Rev.* **177**, 2426 (1969).
- [40] J. S. Bell and R. Jackiw, "A PCAC puzzle: $\pi_0 \rightarrow \gamma\gamma$ in the σ -model", *Il Nuovo Cimento A* **60**, 47 (1969).
- [41] H. B. Nielsen, and M. Ninomiya, "The Adler-Bell-Jackiw anomaly and Weyl fermions in a crystal", *Physics Letters B* **130**, 389 (1983).
- [42] M. M. Vazifeh and M. Franz, "Electromagnetic Response of Weyl Semimetals", *Phys. Rev. Lett.* **111**, 027201 (2013).
- [43] A. Burkov, "Chiral anomaly and transport in Weyl metals", *Journal of Physics: Condensed Matter* **27**, 113201 (2015).
- [44] D. T. Son and B. Z. Spivak, "Chiral anomaly and classical negative magnetoresistance of Weyl metals", *Phys. Rev. B* **88**, 104412 (2013).
- [45] X. Huang, L. Zhao, Y. Long, P. Wang, D. Chen, Z. Yang, H. Liang, M. Xue, H. Weng, Z. Fang, X. Dai, and G. Chen, "Observation of the Chiral-Anomaly-Induced Negative Magnetoresistance in 3D Weyl Semimetal TaAs", *Phys. Rev. X* **5**, 031023 (2015).
- [46] S. K. Donaldson, "The Seiberg-Witten equations and 4-Manifold topology", *Bull. (New Series) of the Amer. Math. Society*, **33**, 45 (1996).
- [47] P. G. O. Freund, "Dirac Monopoles and Witten's Monopole Equations", *J. Math. Phys.* **36**, 2673 (1995).
- [48] C. Adam, B. Muratori, C. Nash, "Non- L^2 solutions to the Seiberg-Witten equations", *J. Math. Phys.* **41**, 5875 (2000).
- [49] M. Loss and H. T. Yau, "Stability of Coulomb systems with magnetic fields: III. Zero energy bound states of the Pauli operator", *Comm. Math. Phys.* **104**, 283 (1986).
- [50] For a symmetry analysis of the Seiberg-Witten monopole equations, see, B. V. Aleynikov and E. A. Tolkachev, "Lie symmetries and particular solutions of Seiberg-Witten equations in R^3 ", *J. Phys.: Math. and Gen.* **36**, 2251 (2003).
- [51] R. A. Mosna, "Singular solutions to the Seiberg-Witten and Freund equations on flat space from an iterative method", *J. Math. Phys.* **47**, 013514 (2006).
- [52] J. W. Morgan, T. S. Mrowka and Z. Szab, "Product formulas along T^3 for Seiberg-Witten invariants" *Math. Res. Lett.* **4**, 915 (1997).

Appendix A: Continuum limit and exactly soluble correlated helimagnet

When $|Q| \ll 2|k_0|$, the low energy effective Hamiltonian for the two Weyl nodes becomes

$$H_{eff} = \int d^3r \sum_{\nu=\pm} (-iv_\nu \psi_\nu^\dagger \boldsymbol{\sigma} \cdot \nabla \psi_\nu + K_0 \mathbf{M} \cdot \mathbf{s}_\nu + \nu b_0) + \dots, \quad (\text{A1})$$

where ν labels the valley of the Weyl nodes, v_ν is the Fermi velocity of the Weyl node ν , and b_0 is the energy offset between the two Weyl nodes caused by the inversion symmetry breaking. The “...” terms include the higher-order terms of derivatives and the exchange terms between \mathbf{M} s. Due to the energy offset b_0 between the two Weyl nodes in a non-centrosymmetric system, we can integrate out one Weyl fermion that is below the chemical potential, say, ψ_- . The effective Hamiltonian is given by (the constant b_0 is omitted) [9, 29]

$$H_{eff} = \int d^3r \left[-i(\psi^\dagger \boldsymbol{\sigma} \cdot \nabla \psi + K_0 \mathbf{M} \cdot \mathbf{s}) + \frac{D}{4} \mathbf{M} \cdot \nabla \times \mathbf{M} + \frac{J}{2} (\nabla \mathbf{M})^2 \right], \quad (\text{A2})$$

where the suffix $+$ is omitted; $J \propto K_0^2 - 2J_0$ and $D \propto v_- K_0^2 + 4D_0$ [15, 16]. We have set $\hbar = v_+ = 1$ and neglected the high-order terms. When $K_0 = 0$, the ground state configuration of the normalized \mathbf{M} is an uncorrelated helimagnet, $\mathbf{M} = [\mathbf{e}_1 \sin(\mathbf{Q} \cdot \mathbf{r} + \varphi_0) \pm \mathbf{e}_2 \cos(\mathbf{Q} \cdot \mathbf{r} + \varphi_0)]$ with $Q = |\mathbf{Q}| = |D/2J|$ and $\mathbf{Q} \propto \mathbf{e}_1 \times \mathbf{e}_2$ [30]. When $K_0 \neq 0$, the spin \mathbf{s} and \mathbf{M} are coupled. The equation of motion for ψ and the ground state configuration of \mathbf{M} satisfy [29]

$$-i\boldsymbol{\sigma} \cdot (\nabla + i\frac{K_0}{2}\mathbf{M})\psi = E_e\psi, \quad (\text{A3})$$

$$K_0 \mathbf{s} + \frac{D}{2} \nabla \times \mathbf{M} - J \nabla^2 \mathbf{M} = 0. \quad (\text{A4})$$

Consider the following ansatz [46–52]:

$$\mathbf{M} = (\sin[Qx], \cos[Qx], 0), \quad (\text{A5})$$

$$\mathbf{B}_0 = (\pm)\frac{K_0}{2} \nabla \times \mathbf{M}, \quad (\text{A6})$$

$$\chi = \frac{e^{iQz/2}}{\sqrt{2(B_0 + B_{03})}} \begin{pmatrix} B_0 + B_{03} \\ B_{01} + iB_{02} \end{pmatrix}. \quad (\text{A7})$$

One can check $\mathbf{B}_0 = \chi^\dagger \boldsymbol{\sigma} \chi$ and $B_0 = \chi^\dagger \chi$. Therefore this provides a map from $SU(2)$ to $SO(3)$. Then the equation of motion for $\psi = \chi/\sqrt{\chi^\dagger \chi}$ reduces to

$$\left(\frac{Q}{2} + \frac{K_0}{2}\right)\psi = E_e\psi, \quad (\text{A8})$$

and the ground state equation for \mathbf{M} reduces to

$$K_0 \mathbf{M} + \frac{DQ}{2} \mathbf{M} - |J|Q^2 \mathbf{M} = 0. \quad (\text{A9})$$

Therefore one obtains

$$Q = \frac{D \pm \sqrt{D^2 + 16|J|K_0}}{4|J|}. \quad (\text{A10})$$

We shall emphasize that although the helical configuration here has the same form as the case for $K_0 = 0$, $|\mathbf{Q}|$ is correlated with the Weyl fermions via the Kondo coupling. It can be proved that the ground state solution can be found for a general helical magnetic configuration $\mathbf{M} = \frac{|Q|}{K_0}(\mathbf{e}_1 \sin(\mathbf{Q} \cdot \mathbf{r} + \phi_0) \pm \mathbf{e}_2 \cos(\mathbf{Q} \cdot \mathbf{r} + \phi_0))$ [29].

We present a more concrete solution with the ansatz $\mathbf{M} = \frac{Q}{K}(\sin[Qz], \cos[Qz], 0)$. Assuming the periodic boundary condition, the spectrum E of the fermions is determined by solving the equation of motion under the effective Hamiltonian (A3):

$$(-i\boldsymbol{\sigma} \cdot \nabla + \boldsymbol{\sigma} \cdot \frac{K}{2}\mathbf{M})\psi = E\psi. \quad (\text{A11})$$

In order to find the zero-energy solution, we focus along one direction, say, the z axis, and take the following ansatz for the wave function:

$$\psi_0(\mathbf{r}) = \psi_n(z) \propto e^{i(k_z + nQ)z} \begin{pmatrix} 1 \\ -\frac{2i}{K}(k_z + nQ - E)e^{-iQz} \end{pmatrix} \quad (\text{A12})$$

where k_z is the wave vector along the z axis, Q is the magnetic wave vector of \mathbf{M} , and n labels the n th magnetic Brillouin zone determined by Q . Then, through a direct calculation, the spectrum reads

$$E_\pm = \frac{Q}{2} \pm \sqrt{(k_z + (n + \frac{1}{2})Q)^2 + \frac{K^2}{4}}. \quad (\text{A13})$$

The zero energy occurs when $|Q| = |K|$ (which is consistent with the normalization $|\mathbf{M}| = 1$), and $k_z = -(n + \frac{1}{2})Q$. The diagram of the spectra (A13) is shown in Fig. 1 of the main text. The spin of these zero modes is the same, i.e., $\mathbf{s}_n = \mathbf{s} = \frac{1}{2}\frac{Q}{K}\mathbf{M}$. Eq. (A4) determines Q as

$$\frac{Q}{2K} + \frac{DQ}{2K} - \frac{|J|Q^2}{K} = 0 \Rightarrow Q = \frac{1}{2|J|}(1 + D), \quad (\text{A14})$$

which also gives a constraint between K and J/D . For a pinned helimagnet with $Q > 0$, say, in the z direction, the dispersion near $k_z = -(n + \frac{1}{2})Q$ for a given zero mode reads,

$$E_-(k_z) \approx -\frac{1}{|K|}(k_z + (n + \frac{1}{2})Q)^2 \equiv -\frac{1}{|K|}q_z^2. \quad (\text{A15})$$

We now perform the perturbation by taking $H_1 = k_x \sigma^x + k_y \sigma^y$ because for the pinned helimagnet, the Hamiltonian (A2) in the main text is translationally invariant in the x - y plane. The first-order perturbation is zero. The matrix

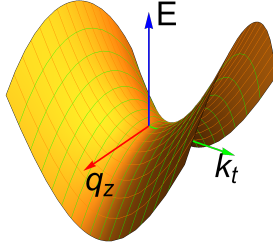


FIG. 5: (color online) A schematic diagram for the dispersion of E_- (A19) near the blue points in Fig. 1. $K = 1$. The dispersion has a saddle shape. It is a parabola along k_t and a downward one along q_z .

elements between

$$\begin{aligned} \psi_{n-}(z) &\propto e^{i(k_z+nQ)z} \begin{pmatrix} 1 \\ -\frac{i2}{K}(k_z+nQ-E_{n-})e^{-iQz} \end{pmatrix} \\ &= e^{i(k_z+nQ)z} \begin{pmatrix} 1 \\ A_n e^{-iQz} \end{pmatrix} \end{aligned}$$

and $\psi_{n'}-(z)$ are

$$\begin{aligned} &\langle \psi_{n'}-(z) | H_1 | \psi_{n-}(z) \rangle \\ &= \delta_{n,n'+1} A_n (k_x - ik_y) + \delta_{n,n'-1} A_{n'} (k_x + ik_y) \end{aligned} \quad (\text{A16})$$

The energy differences at $k_z = -(n + \frac{1}{2})Q$ are

$$E_-(n, k_z) - E_-(n \pm 1, k_z) = \frac{\sqrt{5}-1}{2} K, \quad (\text{A17})$$

The second order perturbation gives

$$\begin{aligned} E_-^{(2)} &= \sum_{n' \neq n} \frac{\langle \psi_{n-}(z) | H_1 | \psi_{n'}-(z) \rangle \langle \psi_{n'}-(z) | H_1 | \psi_{n-}(z) \rangle}{E_n - E_{n'}} \\ &= \frac{2}{\sqrt{5}-1} \frac{k_x^2 + k_y^2}{K}. \end{aligned} \quad (\text{A18})$$

Thus, the dispersions near $k_z = -(n + 1/2)Q$ are

$$\begin{aligned} E_-(\mathbf{k}) &= -\frac{1}{K} q_z^2 + \frac{2}{(\sqrt{5}-1)K} k_t^2 \\ &\equiv -\frac{q_z^2}{2m_z} + \frac{k_t^2}{2m_t} = -\varepsilon_z + \varepsilon_t, \end{aligned} \quad (\text{A19})$$

with $\mathbf{k}_t = (k_x, k_y)$. The dispersion is of a saddle shape (see Fig. 5); namely, in the z direction, it is hole-type, while in the x - y plane, it is particle-type. This means that the dynamics parallel to the helimagnet and perpendicular to the helimagnet are separated.

Appendix B: A brief review of the two-dimensional lattice model in a constant external magnetic field and the Harper equation

Consider a tight-binding Hamiltonian on the square lattice in a magnetic field [31–33]:

$$\begin{aligned} H &= -t_a \sum_{\langle i,j \rangle} c_{x,j}^\dagger c_{x,i} e^{i\theta_{ij}^x} \\ &\quad - t_b \sum_{\langle i,j \rangle} c_{y,j}^\dagger c_{y,i} e^{i\theta_{ij}^y} + h.c., \end{aligned} \quad (\text{B1})$$

where θ_{ij} is the phase factor of the gauge field which satisfies $\sum_{\square} \theta_{ij} = 2\pi\phi$ in a unit cell, and $\phi = p/q$ with p, q coprime. t_a and t_b are the nearest-neighbor hopping constants. A site i on the square lattice has Cartesian coordinates (n, m) where n and m are integers. We choose the gauge $\theta_{ij}^x = 0$, and $\theta_{ij}^y = 2\pi\phi n$ for the link between $i = (n, m)$ and $j = (n, m+1)$. This gauge gives a uniform magnetic field the flux of which through a plaquette is $2\pi\phi$. In the momentum space,

$$\begin{aligned} H(\mathbf{k}) &= -2t_a \cos k_x c^\dagger(k_x, k_y) c(k_x, k_y) \\ &\quad - t_b [e^{-ik_y} c^\dagger(k_x + 2\pi\phi, k_y) c(k_x, k_y) \\ &\quad + e^{ik_y} c^\dagger(k_x - 2\pi\phi, k_y) c(k_x, k_y)], \end{aligned} \quad (\text{B2})$$

where $-\pi \leq k_x, k_y \leq \pi$. Since k_x is coupled to $k_x \pm 2\pi\phi$, the Schrödinger equation $H|\Psi\rangle = E|\psi\rangle$ is reduced to the Harper equation:

$$\begin{aligned} &-t_b (e^{-ik_y} \psi_{j-1} + e^{ik_y} \psi_{j+1}) - 2t_a \cos(k_x^0 + 2\pi\phi j) \psi_j \\ &= E(k_x^0, k_y) \psi_j, \end{aligned} \quad (\text{B3})$$

where $k_x = k_x^0 + 2\pi\phi j$ and $\phi_{j+q} = \phi_j$. And the state $|\Psi\rangle$ is

$$|\Psi\rangle = \sum_{j=1}^q \psi_j c^\dagger(k_x^0 + 2\pi\phi j, k_y) |0\rangle. \quad (\text{B4})$$

Appendix C: Evolution of Weyl nodes with respect to the Kondo coupling K_0

We plot the evolution of Weyl nodes with respect to the Kondo coupling K_0 in Fig. 6. We find that by increasing the Kondo coupling, the Weyl nodes move closer to each other. Finally, they annihilate and open a gap. This process reflects the competition between the monopole topology of the Weyl node and the trivial topology of the helimagnet via Kondo coupling K_0 . For a small K_0 , the Weyl node structure remains stable, while for a large K_0 , the conducting fermions acquire a gap and become trivial.

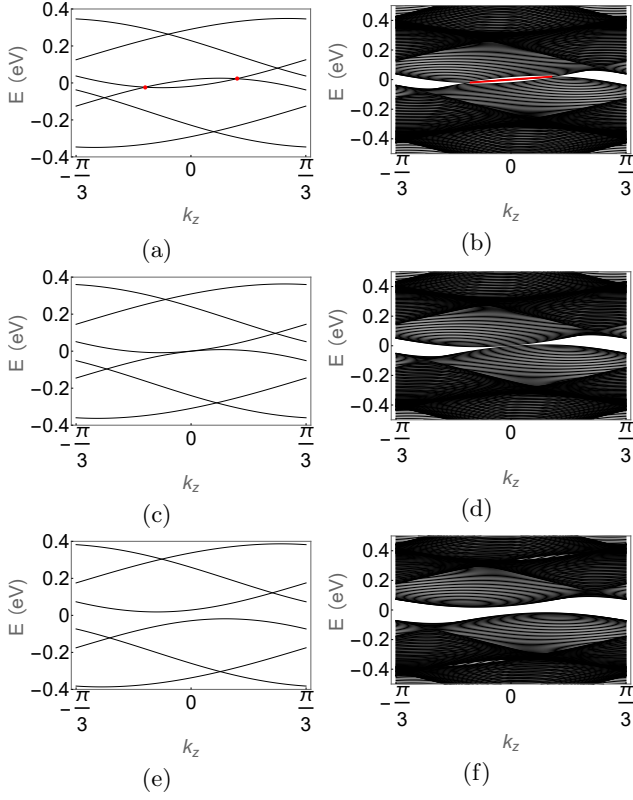


FIG. 6: (Color online) The evolution of Weyl nodes. The parameters are chosen as $Q = 2\pi/3$, $t = t' = 0.1 \text{ eV}$, and $k_x = k_y = 0$. (a) $K_0 = 250 \text{ meV}$, (c) $K_0 = 290 \text{ meV}$, (e) $K_0 = 350 \text{ meV}$. (b), (d), and (f) are the corresponding band structures with open boundary conditions for 50 sites along the y -direction. The red points are Weyl nodes, and the red lines are the Fermi arcs.